

UC Berkeley

UC Berkeley Previously Published Works

Title

Plastic deformation mechanism of calcium-silicate hydrates determined by deviatoric-stress Raman spectroscopy

Permalink

<https://escholarship.org/uc/item/5742q7tz>

Authors

Gardner, David W

Li, Jiaqi

Kunz, Martin

et al.

Publication Date

2021-08-01

DOI

10.1016/j.cemconres.2021.106476

Supplemental Material

<https://escholarship.org/uc/item/5742q7tz#supplemental>

Peer reviewed

1 **Title:** Plastic deformation mechanism of calcium-silicate hydrates determined by deviatoric-
2 stress Raman spectroscopy

3

4 **Authors:** David W. Gardner^a, Jiaqi Li^b, Martin Kunz^c, Chenhui Zhu^c, Paulo J. M. Monteiro^b,
5 Roya Maboudian^a, Carlo Carraro^{a*}

6

7 ^aDepartment of Chemical and Biomolecular Engineering, University of California, Berkeley,
8 Berkeley, CA 94720, United States

9 ^bDepartment of Civil and Environmental Engineering, University of California, Berkeley,
10 Berkeley, CA 94720, United States

11 ^cAdvanced Light Source, Lawrence Berkeley National Laboratory, Berkeley, California 94720,
12 USA

13 *Corresponding author:

14 Carlo Carraro, carraro@berkeley.edu

15 201 Gilman Hall, University of California, Berkeley

16 Berkeley, California 94720

17 United States

18

19 **Keywords:** Calcium-silicate-hydrate; small-angle X-ray scattering; Spectroscopy; Creep;

20 Carbonation

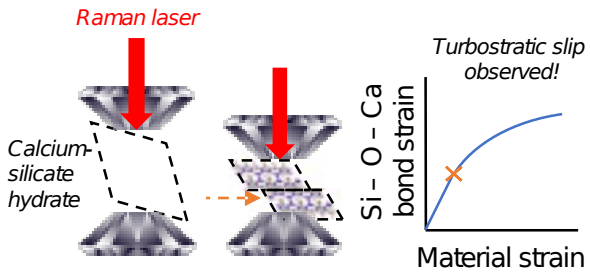
21

22 **Abstract**

23

24 Creep of the cement matrix affects the structural stability of concrete. In Portland cements, the
25 creep is largely controlled by the binding phase calcium-(aluminum-)silicate-hydrate, or C-
26 (A-)S-H. This phase has a lamellar structure and under deviatoric stress aligns its *c*-axis with the
27 principal stress. However, the limiting resistance to this reorientation is unknown at the
28 nanocrystalline level. Small-angle X-ray scattering shows that the lamellae thickness decreases
29 under 100's MPa deviatoric stress. Deviatoric stress Raman spectroscopy shows that there are
30 two ways that this break-up can occur. If the material's silicate chains are cross-linked, then
31 strain in Si-O bonds does not increase above certain stresses, indicating a relaxation adjacent to
32 the Si-O bond. If the chains are not cross-linked, then the silicate chains are broken up by
33 rastering against each other, introducing defects. These results show that the plastic deformation
34 of C-(A-)S-H is relevant for Portland cement creep.

35 **Table of contents image**



36

37 Deviatoric-stress Raman spectroscopy shows how the structure of cement hydrates affects the

38 way they plastically deform.

39 **1. Introduction**

40

41 The long-term deformation of concrete whereby it flows, or “creeps”, under deviatoric stress is
42 important for predicting the life expectancy of the structure and its mechanical properties.

43 Understanding the mechanism of creep could enable designing cement chemistries that have
44 tailored creep compliance. It is desirable to have a high creep value for mass concrete, or any
45 concrete that develops large thermal gradients during the hydration process, because creep
46 alleviates the thermal stress that could initiate cracks. In most structural concretes that are
47 prestressed to strengthen against tension, creep absorbs the prestress and reduces concrete
48 performance, and hence a small creep value is desired.

49

50 Once set, the creep response is largely controlled by the main binding phase in Portland cement,
51 nanocrystalline calcium-(aluminum-)silicate-hydrate (Figure 1). C-(A-)S-H has a layered
52 structure of two-dimensional Ca seven-fold coordinated with O, OH, and H₂O sheets (the
53 “intralayer”) decorated with one-dimensional silicate chains. The uptake of aluminum ions
54 promotes cross-linking of silicate chains on opposite sheets when synthesized above 80 °C [1,2].
55 Between the sheets and the silicate chains are coordinated calcium ions and strongly bound water
56 molecules (the “interlayer”). Standard notation for silica tetrahedra is used here, with Q¹
57 denoting a silica tetrahedron bound only to one other tetrahedron, Q² a silica tetrahedron bound
58 to two others, and Q³ a silica tetrahedron bound to three others.

59

60 In this paper, we compare two types of C-(A-)S-H to understand how their structures affect their
61 mechanical properties. The first type is a cross-linked structure (Figures 1a, c), which contains

62 aluminum. The second is a non-cross-linked sample (Figures 1b, d), which does not. We refer to
 63 these as C-A-S-H and C-S-H, respectively. At the mesoscale, C-(A-)S-H grains have a lamellar,
 64 turbostratic morphology [3] (Figure 1e). This has been established from Rietveld refinement [1],
 65 small-angle X-ray scattering (SAXS) [4,5], and transmission electron microscopy [6]. The short
 66 dimension of a lamella is coincident with the *c*-axis. Around each grain is a several-Å-thick layer
 67 of gel water [7,8].

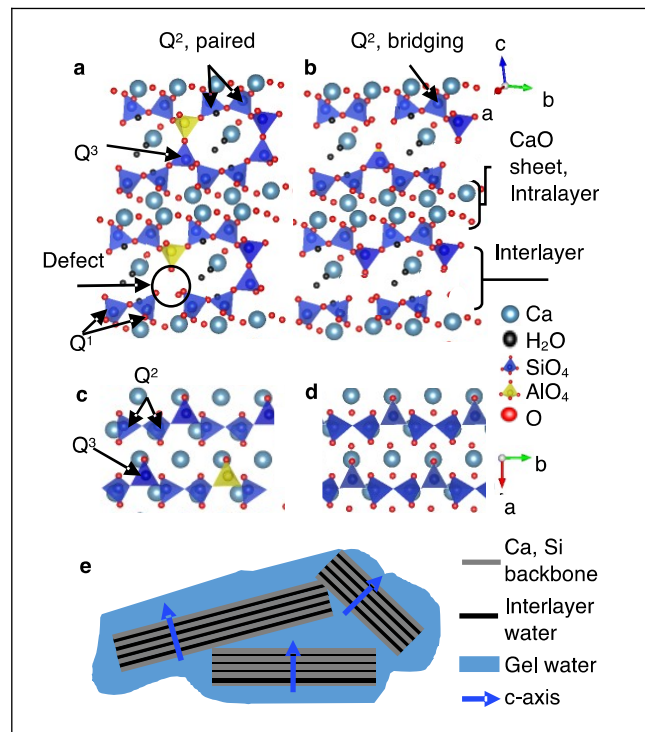


Figure 1: Structure of the calcium-(aluminum-)silicate hydrate (C-(A-)S-H) sample in this work. (a, b) *bc* plane of C-A-S-H and C-S-H, respectively. (c, d) *ab* plane of C-A-S-H and C-S-H, respectively. Half-filled symbols denote half-occupancy in the structure. For simplicity, in the *ab* slice, only the oxygens that are involved in the Si-O

symmetric stretches studied in this work are included, while water molecules, interlayer calcium ions, and the third silicon atom on the Q³ sites are not shown. Both structures adapted from structure of cross-linked 11 Å tobermorite^{5,6}. (e) Simple model of C-(A)-S-H lamellae at the mesoscale, showing the difference between strongly bound interlayer water and surface adsorbed gel water. The *c*-axis of the three grains is drawn. (not to scale)

68

69

70 Under a deviatoric stress the lamellae orient so that the *c*-axis is aligned with the principal

71 compression direction [9], but the mechanism(s) of reorientation remains unclear. For this

72 preferred orientation to develop, either or both of the following must be true: grains slide past

73 each other along their *ab* faces in an intergrain mechanism (“shape preferred orientation”), or a

74 slip plane along the *ab* plane within the crystal is activated in an intragrain mechanism [10]

75 (“lattice preferred orientation”).

76

77 The intergrain resistance is sometimes aided by gel water. Simulations and nanoindentation

78 experiments have shown the lubricating effect gel water has[11–14], especially for thicker water

79 layers, and micro/nanoindentation studies link the creep of cement paste with creep of C-S-H

80 using a semiempirical void-filling model [12,13,15–17]. These semiempirical models are very

81 useful for existing cements, but the models’ fit parameters are not derivable from the structure of

82 the C-S-H, e.g. why C-A-S-H has a lower creep compliance than C-S-H [16]. Grain roughness
83 [18] could also play a role, although this parameter is difficult to measure directly. The barriers to
84 movement at low relative humidity or low porosity remain unknown.

85

86 Intragrain resistances are plausible given that C-(A-)S-H has a similar structure to micas, a
87 layered clay mineral, which require only 100's MPa to activate sliding on the *ab* plane [19,20].
88 The analogy to micas is consistent with computations showing that the lowest energy plane to
89 expose in 11 Å tobermorite is the (004) plane [21], which coincides with the intralayer.

90

91 In this paper, we present results obtained from compacted pellets of C-S-H and C-A-S-H
92 prepared using uniaxial stresses of 740 MPa. We track changes in their grain size with SAXS.
93 We observe a decrease in grain thickness from ~70 Å to ~50 Å in both samples after they have
94 been subjected to 740 MPa uniaxial compression. We do not observe any decrease in effective
95 radius. The plastic deformation observed by SAXS signals bond-breaking events. Therefore, we
96 probe the chemical environment of the silicate tetrahedra with Raman spectroscopy, both ex-situ
97 and in-situ during compaction with Raman spectroscopy in a diamond anvil cell. We find that in
98 the C-A-S-H sample under high stresses, the Raman peak corresponding to the Si – O –
99 Ca(intralayer) stretch does not increase in vibrational energy, meaning that its bond strain does
100 not increase, while the interlayer Si – O – Si bending peak does increase in energy. This
101 indicates a relaxation of the intralayer in C-A-S-H. In contrast, both of these bonds develop
102 strain in the C-S-H sample, suggesting that the slip plane in C-S-H is the water-rich interlayer,
103 *not* the intralayer. The deviatoric stress Raman spectroscopy experiments show that the slip plane

104 that leads to a decrease in grain thickness is different between cross-linked C-A-S-H and non-
105 cross-linked C-S-H.

106

107 **2. Methods**

108

109 **2.1 Samples**

110

111 The C-(A-)S-H powders were synthesized by a standard method described elsewhere [9]. Briefly,
112 samples were synthesized at 80 °C for 56 days with Ca to Si reagent ratio of 1.0, and in the case
113 of the C-A-S-H samples, with Al/Si = 0.1. Note that while X-ray diffraction (XRD) of the C-S-H
114 sample (Figure S1) shows that the (002) basal peak that can be deconvoluted into two basal
115 peaks, with thicknesses 24.4 Å and 27.6 Å, we treat this sample as homogeneous in the 24.4 Å
116 because this spacing is five times more abundant. The basal spacing of the C-A-S-H is 11.6 Å.
117 Samples were stored in vacuum box when not in use. Previous NMR characterizations of these
118 samples are provided elsewhere [2], showing 17% Q¹ in the C-A-S-H and 23% Q¹ in the C-S-H,
119 and 14% Q³ in the C-A-S-H and 0% Q³ in the C-S-H. The mean chain length in the C-A-S-H is
120 19.8 and is 8.8 in the C-S-H.

121

122 **2.2 Pellet pressing**

123

124 Pressed pellets of the samples were formed by loading the powder into a die and applying 740
125 MPa uniaxial stress in a pellet press for 60 seconds. Previous XRD experiments have shown that

126 the response to such a high uniaxial stress is quite fast [9]. We define pressure and deviatoric
127 stress as in Equations 1, 2:

$$P = \frac{1}{3} * (\sigma_s + 2 * \sigma_T) \quad (1)$$

$$S = \frac{1}{3} * (\sigma_s - \sigma_T) \quad (2)$$

128

129 where P is the hydrostatic pressure, σ_s is the uniaxial stress, σ_T is the average transverse stress,
130 and S is the deviatoric stress.

131

132 The uniaxial stress of 740 MPa was chosen to enable comparison with previous high-pressure
133 deviatoric stress XRD results [9] and the stresses accessible by the deviatoric-stress Raman
134 spectroscopy system described below. Lower stresses have larger uncertainty because of the
135 lower accuracy at such stresses. Higher stresses were not accessible because of the mechanical
136 limit of the stainless steel die used.

137

138 The 740 MPa uniaxial stress (σ_s) applied to the powder to form the pellet is less than the
139 deviatoric stress felt by the powder in the diamond anvil cell experiments. Applying an effective
140 Poisson ratio to the powder of 0.3 [22,23] leads to a transverse stress (σ_T) equal to ~300 MPa
141 and a deviatoric stress of 130 MPa while forming the pellet. This estimate of the deviatoric stress
142 S is an upper bound because the effective Poisson ratio for powders is greater than the value for a
143 solid material.

144

145 The pressed pellet method was chosen because it allows the collection of a large volume of
146 sample to be readily analyzed by the synchrotron beamline described below. Aligning a sample
147 that had come from a diamond anvil cell gasket is practically impossible because samples
148 become cemented with the gasket.

149

150 **2.3 Small-angle X-ray scattering**

151

152 Small-angle X-ray scattering (SAXS) were carried out at beamline 7.3.3 at the Advanced Light
153 Source at Lawrence Berkeley National Lab with a beam energy $E = 10$ keV, a bandwidth $\Delta E/E =$
154 1% and a beam size about $300 \times 700 \mu\text{m}^2$ with a q -range between 0.004 and 0.4 \AA^{-1} . Pressed
155 pellets were loaded into 1 mm diameter capillaries by lightly breaking up the pellet by hand in a
156 mortar and pestle and collecting the powder into a capillary. Scattering patterns were recorded on
157 a two-dimensional Pilatus 2M detector (Dectris), which has a pixel size of $172 \mu\text{m}$. The exposure
158 time used was less than five seconds. The X-ray beam position on the detector and the sample to
159 detector distance were calibrated using the standard silver behenate. The two-dimensional data
160 were calibrated and azimuthally averaged into one-dimensional intensity, I , vs. scattering vector,
161 q , using Igor Pro Nika package [24]. The 1D data were analyzed by numerically integrating the
162 full form factor for a disk [25], assuming a discretized normal distribution of thicknesses (i.e.
163 contribution only from integer multiples of the basal spacing) and with a constant aspect ratio for
164 each sample (Equations 3a-3e):

165

$$I(q) = I_0 \sum_{i=1}^{inf.} F_i^2(q) * S(q) * Weight(i \text{ basal spacings}) \quad (3a)$$

$$\text{Weight}(i \text{ basal spacings}) = \exp\left(\frac{-(i-\mu)^2}{2\sigma^2}\right) \quad (3b)$$

$$F_i^2(q) = \int_0^{\pi/2} |\hat{u}| \hat{u} \quad (3c)$$

$$T_i = 0.5 * i * \text{basal spacing} \quad (3d)$$

$$\text{Aspect ratio} = \frac{R_i}{T_i} = \text{constant} \quad (3e)$$

166

167 where $I(q)$ is the intensity at the scattering vector q , I_0 is an intensity factor, $S(q)$ is the static

168 structure factor, $F_i(q)$ is the single particle form factor, i is an index for the number of basal

169 spacings in the grain, μ is the mean number of basal spacings, σ is the standard deviation of the

170 distribution, T_i is half the sample thickness, R_i is the average particle radius (related to the

171 thickness by the aspect ratio), ϕ is the angle between the normal to the disk plane and the

172 scattering vector q .

173

174 A constant aspect ratio assumption is preferred over a constant radius assumption because (i) it is

175 more physical based on equilibrium crystal shapes, and (ii) the constant aspect ratio assumption

176 gives a better fit. In this fit, the scale factor, the average thickness, and the sample aspect ratio are

177 the only fit parameters. The fit thickness is nearly the same if an empirical Guinier-Porod model

178 [4,26] is applied, although the goodness-of-fit is better using the full form factor. The full form

179 factor also has the advantage of giving a stable fit grain radius to varied starting conditions,

180 whereas the empirical model does not have the q -range to fit the average grain radius.

181

182 The results were highly reproducible within a single sample. Representative fits for each sample

183 are given in Figure S2. The error for least-squares fitting was defined as: $\text{Error}(I(q)) = \log(I(q))$,

184 experiment) – $\log(I(q), \text{fit})^2$. The $\log(I(q))$ operation is needed because of the power-law
185 dependence of the scattering.

186

187 The fitting procedure was taken after Ref. [27], which studied sheet silicates with various
188 intercalates. First, the patterns were fit to Equations (3a-3e) assuming $S(q) = 1$, i.e. assuming no
189 interparticle orientation effects or a dilute suspension. This assumption is a useful for the first fit
190 because form factor scattering dominates the pattern, and because as will be shown below, there
191 are very weak oscillations or peaks from interparticle scattering that would corrupt our
192 regression. Once the pattern has been fit, the measured intensity $I(q)$ is divided by the fit form
193 factor intensity $F^2(q)$ to yield an effective $S(q)$ [27].

194

195 **2.4 Ambient Raman spectroscopy**

196

197 Ambient Raman spectra were recorded by loading the powder or pellet onto a glass slide. The
198 spectra were acquired in backscattering geometry at room temperature with a JY-Horiba Labram
199 spectrometer with an 1800 groove/mm grating. A HeNe laser (632.8 nm) provided the excitation
200 line through an Olympus BX41 confocal microscope, which was focused on the sample by a 50x
201 long working distance objective (Olympus SLMPLN 50x objective, focal length = 180 mm). The
202 spot size was less than 1 μm . Peak assignments for vibrations considered in this work are given
203 in Table 4. Standard deviation of the measured peak centers is 0.8 cm^{-1} for the Q^2 bending peak
204 and 1.2 cm^{-1} for the Q^2 stretching peaks in both samples. Typical standard error of the fit peak
205 center is 1 cm^{-1} . Incorporation of Al in C-A-S-H does not lead to meaningful increases in peak
206 width compared to the C-S-H sample [28,29].

207 **Table 4.** Peak assignments for Raman spectroscopy of
 208 calcium-aluminum-silicate hydrates relevant to this
 209 work.

210 Ambient position (cm ⁻¹)	Assignment [28,30-33]
211 675	Si-O-Si Q ² bending
212 850	Si-O-X Q ¹ symmetric stretch
212 1010	Si-O-X* Q ² symmetric stretch
213 1075	CaCO ₃
214 *X ≠ Si, Al	

2.5 High-pressure and deviatoric stress Raman spectroscopy

The experiments described below were performed on the same Raman spectrometer described in section

2.4. Hydrostatic high-pressure

215 Raman spectra were acquired by loading the sample into a BX90 diamond anvil cell by a
 216 standard procedure with a pressure medium, either a 4:1 volume/volume mixture of methanol to
 217 ethanol, or silicone oil [34]. It was necessary to use multiple pressure media so that the sample
 218 peaks could be observed without interference from the pressure media peaks [29]. Methanol-
 219 ethanol mixtures have interfering peaks around 1000 cm⁻¹, while silicone oil has an interfering
 220 peak around 650-700 cm⁻¹. Typical exposure times were 20 minutes with a 10 mW laser. The
 221 power of the laser is defined at the source. The standard ruby lines could not be used for
 222 hydrostatic pressure measurement when measuring the minerals in this study because the high
 223 laser power needed for the calcium silicate hydrate samples activates the ruby fluorescence,
 224 resulting in unacceptable convolution with the samples' weak Raman lines. Instead, the pressure
 225 in the diamond anvil cell was obtained from the Raman frequency of the top diamond culet, as
 226 described elsewhere [29].

227

228 Deviatoric stress Raman spectra were acquired by lightly packing the powder into a BX90
 229 diamond anvil cell in a stainless steel gasket, with multiple well-spaced ruby spheres loaded onto

230 the top diamond before assembling the diamond anvil cell (Figure 2). We were able to record
231 the spectra of C-(A-)S-H in the diamond anvil cell under deviatoric stress despite rubies in the
232 sample chamber because the compaction of the sample by the deviatoric stress increases the
233 packing density of the C-(A-)S-H powder and therefore the signal is strong enough to be seen. A
234 spot in the gasket was consistently sampled throughout the deviatoric stress experiments. C-
235 (A-)S-H Raman spectra were deconvoluted with CasaXPS software using mixed Gaussian-
236 Lorentzian functions. Typical standard error from the regression of the peak center is 2.0 cm^{-1} for
237 both peaks for spectra recorded in a diamond anvil cell.

238

239 Although peak widths increase by $\sim 30\%$ in the diamond anvil cell when the material is under
240 pressure and the grains may deform their shape, the regression uncertainty for the peak center
241 remains roughly 2.0 cm^{-1} for the pressure range studied here in hydrostatic and deviatoric
242 conditions.

243

244 When combining the separately obtained Q^2 bending and stretching peaks, as in the hydrostatic
245 points of Figure 5, a linear relationship between wavenumber and pressure was assumed for one
246 mode – in the C-S-H sample, the Q^2 bending peak, and in the C-A-S-H sample, the Q^2 symmetric
247 stretch peak [29]. The frequency of that mode was estimated at the pressure of the other mode.

248

249 The error bars for the hydrostatic points in Figure 5 are either the contributions from the
250 spectrometer imprecision, repeatability uncertainty, and peak fit center standard error; or two
251 standard errors of the regression line between the Q^2 bending peak with pressure in C-S-H (two
252 standard errors = 3.00 cm^{-1}) or between the Q^2 symmetric stretching peak in C-A-S-H with

253 pressure (two standard errors = 5.81 cm⁻¹). Different modes were used as the basis for the plot
254 because the linearity between peak center and pressure was better for different modes between
255 the two samples. These plots are available from our previous work[29].

256

257 Calcium oxide vibrations at low wavenumbers were not resolvable in the diamond anvil cell,
258 neither were Q³ bending vibrations seen in tobermorites[30] (Figure S8, S9). Q³ vibrations are
259 not intense enough to observe by Raman spectroscopy even though these tetrahedra are present
260 in the C-A-S-H sample[2,29].

261

262 **2.6 Determining stress field in deviatoric stress Raman spectroscopy**

263

264 Components of hydrostatic pressure P and deviatoric stress S were determined by the shift in the
265 ruby R₂ line and by the difference between the R₁ and R₂ lines, respectively [35] (Figure S3). The
266 ruby R₂ wavelength depends only on pressure within the deviatoric stress range in this study
267 [35]. Ruby R₁, R₂ peak positions were determined by deconvolution with CasaXPS software
268 using pure Lorentzian functions. The equations used to calculate P and S as functions of the R₁
269 and R₂ wavelengths are given in the SI, Equations ES1-ES2.

270

271 Deviatoric stress naturally arises in
272 powder samples in the diamond
273 anvil cell with the stress along the
274 direction normal to the diamonds
275 being greater than the transverse
276 stress imposed by the gasket.

277 Although we cannot control the
278 initial orientation of the ruby
279 spheres, we observe that all five
280 rubies show an increase in the
281 wavelength difference between the
282 two peaks once deviatoric stress is
283 applied (Figure S4), leading us to
284 conclude that the rubies are oriented
285 with their *a*-axis nearly along the

286 direction of the stress [35]. The magnitude of the reported stress should therefore be considered
287 an upper bound of the stress felt by the ruby. We define pressure and deviatoric stress as in
288 Equations (1) and (2).

289

290 The uniaxial stress is the stress along the axis of the diamonds. We calculate these properties in
291 the rubies[35], take the average result, and assume this stress field being felt by the powder. This
292 “equal-stress” assumption for every grain in the diamond anvil cell (also known as the Reuss

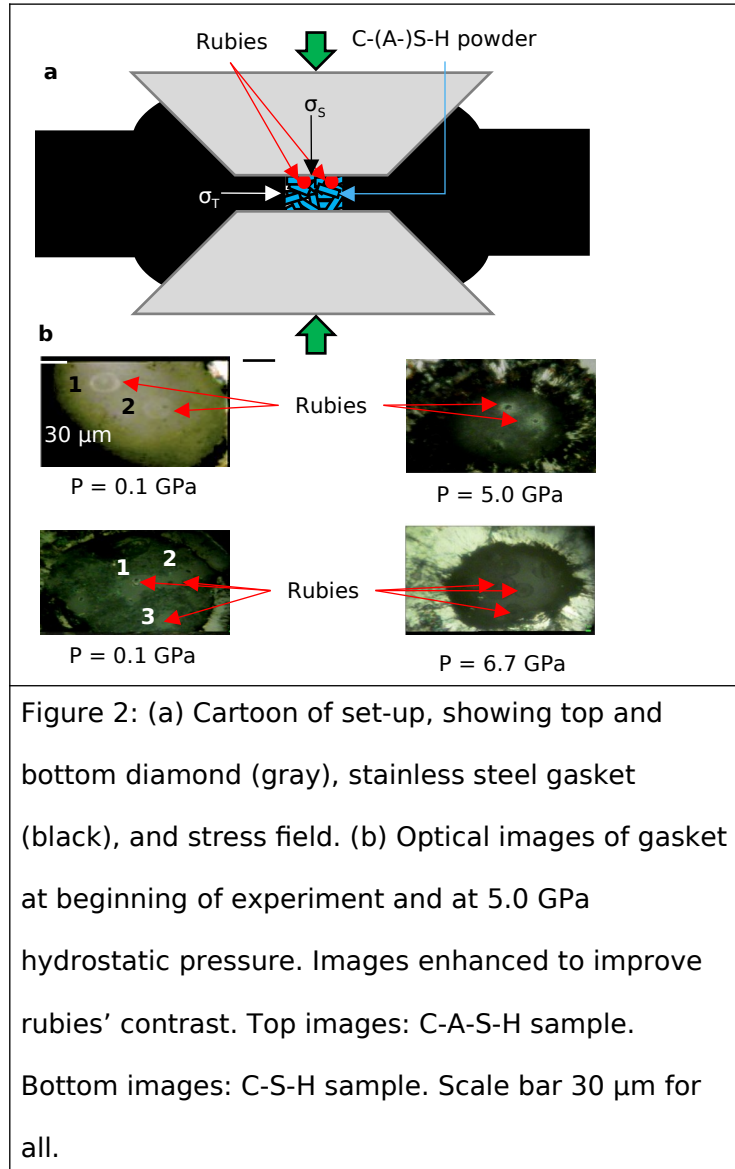


Figure 2: (a) Cartoon of set-up, showing top and bottom diamond (gray), stainless steel gasket (black), and stress field. (b) Optical images of gasket at beginning of experiment and at 5.0 GPa hydrostatic pressure. Images enhanced to improve rubies' contrast. Top images: C-A-S-H sample. Bottom images: C-S-H sample. Scale bar $30 \mu\text{m}$ for all.

293 approximation) is standard in geophysics and materials research using diamond anvil cells under
294 deviatoric stress [9,36,37].

295

296 **2.7 Theory of deviatoric-stress Raman spectroscopy applied to C-(A-)S-H**

297

298 Raman spectroscopy in a diamond anvil cell is used to study chemical bond strain while
299 deviatoric stress is applied. To understand how to interpret deviatoric-stress Raman spectra, it is
300 necessary to start from hydrostatic Raman spectroscopy.

301

302 The key concept of hydrostatic Raman spectroscopy is that chemical bonds have characteristic
303 anharmonicity γ_i , also known as the mode Grüneisen parameter, which is the relative change in
304 the relative vibrational frequency with the strain of the vibration [38], in Equation 4:

$$\gamma_i = \frac{-d \log(\omega_i/\omega_0)}{d \log(V_i/V_0)} \quad (4)$$

305 where i is an index indicating the calculation is for a particular bond, 0 is an index indicating the
306 ambient value, ω is the frequency of the chemical bond vibration and V is the average volume of
307 the chemical bond that changes with pressure. The value of the anharmonicity is not necessarily
308 the same over a large strain range, but vibrational mode frequency and vibrational mode volume
309 are always linked.

310

311 The mode Grüneisen parameter can be measured when high-pressure X-ray diffraction data are
312 combined with separately obtained high-pressure Raman data. In simple structures with only one
313 or two characteristic interatomic distances, the volume change of the bond with pressure can be

314 rigorously (and trivially) assigned to the volume change of the unit cell. In more complex unit
315 cells, the volume change is rigorously assigned to the *volume of the oscillation* that changes
316 under compression [38]. We have previously discussed how this analysis can be used to learn
317 about bond characteristics in C-(A-)S-H towards improved force fields and designing new
318 cements [29]. In this work we invert the relation in Eq. 4 to note that the frequency has a
319 characteristic relationship to volume strain.

320

321 The Q² symmetric stretch at $\omega_0 \sim 1000 \text{ cm}^{-1}$ is in a plane nearly perpendicular to the b-axis and
322 with the CaO intralayer. We will call the intralayer *c_intralayer*. The distinction between the
323 entire axis *c* and the *c_intralayer* is necessary because the compressibilities are so different [34].
324 The intralayer volume change is proportional to the area of the *a-c_intralayer* plane to a good
325 approximation. The Q² bending at $\omega_0 \sim 670 \text{ cm}^{-1}$ is bending between the *b*-axis and *c*-axis, so its
326 volume change is proportional to the area of the *bc* plane. Garbev et al. noted that Q² bending
327 frequency increased as the paired angle decreased [32] in crystalline calcium silicate phases. Our
328 earlier work with hydrostatic Raman spectra in C-S-H [29] showed this frequency monotonically
329 increasing, which suggests that the bond angle should be decreasing, as some calculations of C-
330 S-H phases suggest [34]. However, correlations that are observed between crystalline phases will
331 not necessarily hold within a phase as it is compacted.

332

333 The error bars in the strain for the hydrostatic points were determined by using two standard
334 errors of the pressure uncertainty ($\sim 0.16 \text{ GPa}$ [29]) and applying this to the compliance tensor,
335 always assuming a hydrostatic condition. The error bars of the strain for the deviatoric points
336 were determined with two sample standard deviations of the stress field. For more details, see the

337 supplementary material, Equations ES3-ES10. The assumptions we have applied have led to the
338 widest reasonable error bars.

339

340 The compliance tensor is applied assuming that all *c*-axes are oriented perfectly towards the
341 diamond axis – and given that nearly all of the grains are oriented within 20° of the deviatoric
342 stress vector at ~800 MPa uniaxial stress[9], this assumption is reasonable. The assumption
343 means that *c*-strains are overestimated in the deviatoric case, especially for the first few data
344 points when grains have not yet ordered, because the *c*-axis strain is the most sensitive to
345 orientation in the stress field. This has only a small effect on the C-A-S-H sample, because its
346 compliance tensor is fairly isotropic. In the C-S-H sample the orientation assumption probably
347 overestimates the strain in the *c*-axis, because the *c*-axis is the softest axis in the material.

348

349 The deviation between *mode strain* and *unit cell strain* has to be observed by comparing the
350 vibrational frequency at a particular unit cell strain for two conditions. The first condition is
351 hydrostatic, with only elastic deformation (in our case, in pressures of at least 10 GPa in a
352 pressure medium). This assertion is made by observation that the diffraction pattern of the
353 samples is nearly identical after unloading the sample from a DAC during a high-pressure XRD
354 experiment [1]. The second condition is a deviatoric stress high enough to cause plastic
355 deformation.

356

357 To summarize: vibrational mode strain is linked to vibrational mode frequency. If the mode
358 strain is evolving differently under conditions known to cause plastic deformation (i.e.,
359 deviatoric stress) vs. conditions where there is no plastic deformation (i.e., hydrostatic), *after*

360 *accounting for the unit cell strain*, then that mode is identified as being linked to the plastic
361 deformation.

362

363 **2.8 Deviatoric stress Raman spectroscopy: Stress field in diamond anvil cells**

364

365 In this experiment, powders are loaded into a gasket with several rubies as stress field gauges and
366 the powders' Raman spectra are measured at each tightening position. The pressure and
367 deviatoric stress felt by each ruby at each measurement point and the average condition applied
368 to the powders are given in Figure 3a-3f for both samples. The agreement is quite reasonable for
369 diamond anvil cell work, with a standard deviation of 0.4 GPa for pressure and 0.5 GPa for
370 deviatoric stress between rubies at a particular measurement for both experiments. The
371 magnitude of the deviatoric stress agrees well with the results of Geng et al., where a similar
372 loading setup was used for high-pressure X-ray diffraction experiments [9].

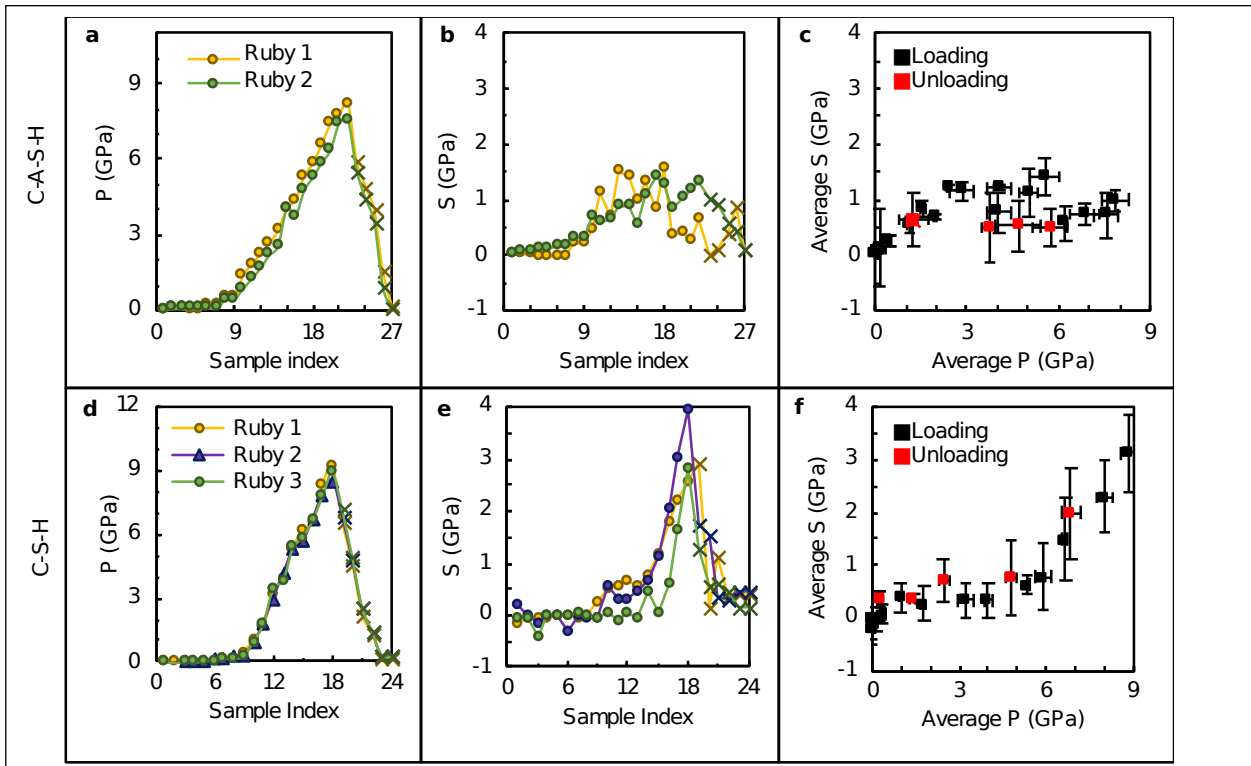


Figure 3: Stress field in the diamond anvil cell as determined by rubies. Unless otherwise noted, cross marks indicate unloading. (a) Pressure in gasket for C-A-S-H experiment. (b) Deviatoric stress in gasket for C-A-S-H experiment. (c) Comparison of stress and pressure throughout experiment, error bars are one standard deviation of standard values. (d) Pressure in gasket for C-S-H experiment. (e) Deviatoric stress in gasket for C-S-H experiment. (f) Comparison of stress and pressure throughout C-S-H experiment, error bars are one standard deviation of measured values.

373

374

375 All five ruby spheres' R_1 and R_2 lines separated at high stresses, indicating that their a -axes are

376 aligned with the principal stress. The a -axis is softer in ruby for pressures less than 6 GPa [39],

377 and samples tend to align their softest axis with the principal axis of stress.

378

379 Some of the rubies' lines actually decreased the separation at early stages of compaction (Figure
380 S4), which manifests as a negative calculated deviatoric stress component, e.g. Ruby 1, Figure
381 3b, and Ruby 3, Figure 3e. This indicates that at early stages this ruby's *a*-axis was not aligned
382 with the principal axis of stress, but as the powder tugged at the ruby during compaction, the
383 softest axis of the ruby (the *a*-axis) was pulled into alignment with the principal axis of stress.

384

385 **2.9 Determining unit cell strain in samples under non-uniform stress field**

386

387 The generalized Hooke's Law was used to estimate the relative change in the cell axis length.

388 The compliance tensors were calculated with CSH-FF and taken from Ref. [9]. The tensor

389 developed for C-A-S-H sample compares well with actual mechanical properties of the sample.

390 The tensor developed for C-S-H in Ref. [2] compares well with the dominant phase in the C-S-H

391 samples (sample number A10_C1 in Ref. [1]). The generalized Hooke's law is given in Equation

392 5:

$$Strain_{kl} = C_{ijkl}^{-1} \cdot Stress_{ij} \quad (5)$$

393

394 where *kl* is a crystal or sample axis (i.e., 11, 12, ...), C_{ijkl} is the full (36-component) compliance

395 tensor, and *ij* is a stress direction *from the reference of the sample*. In the hydrostatic case, the

396 stress is uniform everywhere and there is no bulk shear stress, so the point of reference does not

397 affect the analysis.

398

399 In the deviatoric case the stress is not uniform everywhere, so reconciliation of the stress axes

400 and the sample axes is not guaranteed. However, these samples show very large preferred

401 orientation under deviatoric stress, with a large fraction of the crystals aligning their 33 or *c* axis
402 towards the largest component of the stress field [9].

403

404 3 Results and Discussion

405

406 3.1 Small-angle X-ray scattering of pressed pellets

407

408 To investigate the effect of deviatoric stress on grain size, we compacted C-(A-)S-H powders
409 with a uniaxial stress of 740 MPa in a die in a pellet press and compared the small-angle X-ray
410 scattering (SAXS) spectra before and after. Representative sample spectra $I(q)$ after subtracting
411 capillary background are given in Figure S2, and normalized spectra are given in Figures 4a, b.
412 (See Methods section for further details.) The average thickness of the grains and the range of
413 thicknesses in each case are given in Table 1. We do not find any difference between the C-A-S-
414 H and C-S-H powder lamellae thicknesses. Differences in radii between the powders are not
415 statistically significant.

416

Table 1. Fit parameters in small angle scattering. Values in parentheses are one standard error, including the standard error of fit values and standard deviation of measured values. The definitions of μ , σ , and aspect ratio are given in Equations 3a-3e.

Sample	Average thickness, $2 * T$ (Å)	Standard deviation, σ (Å)	$2 * \text{Average Radius}$ (Å)	Aspect ratio, R/T (-)
C-A-S-H Powder	69.1 (3.5)	16.5 (1.0)	1060	0.065

				(151)	(0.006)
	Pellet, 740 MPa	47.5 (4.2)	10.8 (1.6)	931 (82)	0.051 (0.000)
C-S-H	Powder	73.4 (1.0)	17.9 (0.3)	1165 (16)	0.063 (0.000)
	Pellet, 740 MPa	47.8 (1.4)	10.9 (0.4)	870 (57)	0.055 (0.002)

417

418 The fit parameters in Table 1 from SAXS compare well with the parameters obtained by Geng et
419 al. [1] as a byproduct of their Rietveld refinement, which provides an estimate of the size of the
420 coherent scattering domain along an X-ray scattering vector. The thickness of the C-A-S-H
421 sample by SAXS is nearly identical to the value obtained with Rietveld refinement (69.1 Å here
422 vs 75 Å by Geng); however, the C-S-H sample appears much thicker here than by Rietveld
423 refinement (73.4 Å vs. 35 Å by Geng). The difference arises because XRD peak widths used for
424 Rietveld refinement are related to the mean coherent scattering length, whereas SAXS is agnostic
425 to the crystallinity of the sample. The C-S-H sample has more defect sites (as Q^1) than the C-A-
426 S-H sample so this is the most likely explanation for the large difference with XRD analysis in
427 the C-S-H samples.

428

429 Figures 4a, b normalize the intensity with a factor of q^4 . This normalization is used to make
430 changes in grain thickness more apparent for visual inspection. In a Guinier-Porod model [26],
431 the thickness of a disk is essentially determined the scattering vector where the intensity switches
432 from being proportional to q^4 to q^2 . The further to the right this bend is, the thinner the disks.

433 Figures 4a, b show that this bend is further to the right in the pellet samples, indicating that the
 434 lamellae are broken up by the compaction process.
 435
 436 Grain-grain correlations in sheet silicates manifest as ripples in a plot of intensity divided by the
 437 fit form factor, $I(q)/F^2(q)$, which is effectively a fit $S(q)$ [27] (Figures 4c, d). In general, $S(q)$
 438 oscillates about 1.0 for all samples, meaning that interparticle distances and orientation effects
 439 are simply too varied to generate characteristic ripples. However, there are a few exceptions to
 440 this. First, there appears to be a peak in the pellets (red traces) at $q \sim 0.06 \text{ \AA}^{-1}$ (red dashed line in
 441 Figures 4c, d). Inspecting the fits, it is clear that this peak just an artifact of the fit, where the fit
 442 profile expects peaks where there are none (Figure S2).
 443

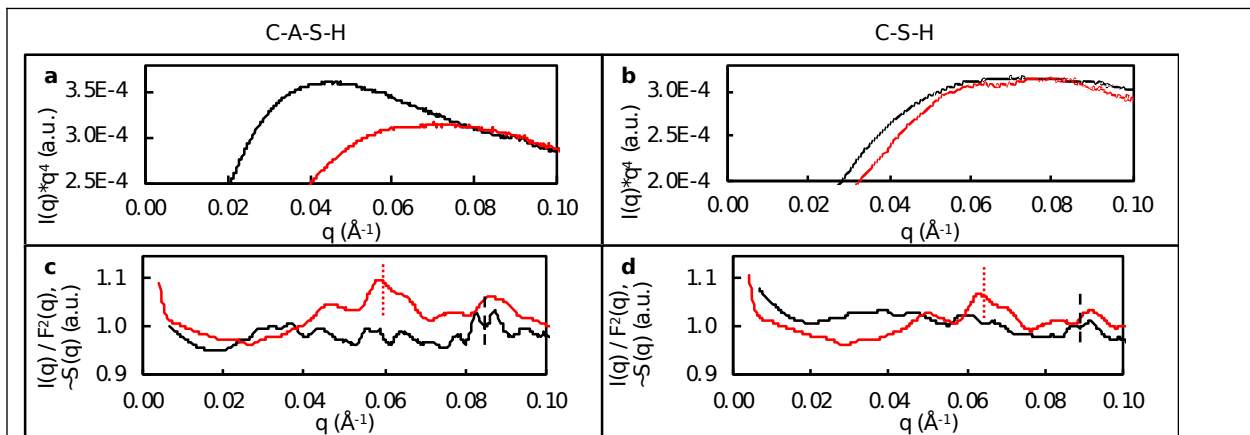


Figure 4: SAXS of C-A-S-H and C-S-H powders subjected to loading conditions. Spectra have had capillary background subtracted and been rescaled. (a, b) q^4 -normalized scattering intensity of powder and crushed pellet for easier inspection to determine grain thickness in C-A-S-H and C-S-H, respectively. (c, d) Effective interparticle structure factor $S(q)$ for powder and crushed pellet. Red dashed lines mark an artifact of the fit; black dashed lines mark intergrain spacing.

444

445 The second notable feature is the doublet at $q \sim 0.09 \text{ \AA}^{-1}$ in the powder samples (black dashed
446 line in Figures 4c, d). This feature is present in the measured $I(q)$, and is present at the same
447 scattering vector for both samples (Figure S5), and is not present after compaction. This peak
448 likely corresponds to some local minima for opposing charged particles separated by either air or
449 gel water, and has been observed experimentally for sheet silicates in various solvents [27]. The
450 scattering vector magnitude corresponds to a particle-to-particle distance of 70 \AA , which is
451 roughly the size of the particles. This intensity is not observed in an empty capillary's pattern
452 (Figure S6). Local minima for interparticle spacing on the order of 10 's – 100 's \AA are common
453 in colloidal systems, and to our knowledge this is the first direct experimental evidence of such a
454 stable spacing for C-S-H in the powder phase, vindicating several calculations predicting a
455 similar value [40,41]. The similarity in value of the magnitude of the scattering vector for both
456 samples is a result of their homologous structures; both are expected to expose the intralayer
457 (004) plane [21,42]. The third notable feature is the broad peak in $I(q)/F^2(q)$ around $q \sim 0.04 \text{ \AA}^{-1}$.
458 This is a grain-grain correlation, as it is present at roughly $q = 2\pi/2T$ [43], and corresponds to
459 grains stacked on top of one another.

460

461 Compaction generally leads to more long range order[44], which should manifest as intense
462 ripples in a SAXS pattern, yet the SAXS pattern of the compacted pellets shows no ripples, and
463 the only “peaks” in the effective $S(q)$ are annihilated by the compaction. This paradox is resolved
464 by the inhomogeneity of lamellae dimensions and the spacings between lamellae in the
465 compacted powders. The compaction at 740 MPa imparts enough stress on the lamellae to break
466 them apart and disrupts the stable 70 \AA spacing structure from the powder. The heterogeneity of
467 the compaction prevents intensity from building up at any characteristic q [43]. Further

468 experiments based on X-ray diffraction patterns of compacted C-S-H may yield more detailed
469 insights to the compaction mechanism.

470

471 SAXS pattern of the samples show a decreased thickness in pressed pellets, but it is unknown
472 how this occurred at a chemical-bond level. To answer this question, we used Raman
473 spectroscopy to track bond strain and the relative population of silica tetrahedra of C-(A-)S-H
474 powders under deviatoric stress.

475

476 **3.2 High-pressure Hydrostatic and Deviatoric Raman Spectroscopy**

477

478 The evolution of the silicate mode frequencies with pressure was measured using Raman
479 spectroscopy. The mode frequency is closely tied to the mode strain. As the volume of the mode
480 decreases with compaction, the frequency and the associated Raman shift increase. Applying the
481 stress field from the rubies to the compliance tensor of the material shows that once the powders
482 are compacted in the cell (i.e. after sample index 9 in Figure 3) all of the crystal axes decrease in
483 length.

484 Figure 5 displays the silicate mode frequencies under deviatoric stress and hydrostatic
485 stress, conditions that lead to plastic and elastic strain, respectively. (For mode frequencies
486 versus pressure, see Figure S7a-d; for mode frequencies versus estimated unit cell strain, see
487 Figure S7e-h). Pressure coefficients are given in Table 2. Representative raw data for the
488 hydrostatic and deviatoric loads can be found on Figures S8, S9. Further discussion of
489 hydrostatic pressure Raman spectra is given in Ref. [29]. Strikingly, in the C-A-S-H sample, the
490 Q^2 Si – O symmetric stretch strain diverges from the Q^2 Si – O – Si bending strain in the

491 deviatoric condition, while the C-S-H sample shows essentially the same relative increase in
492 mode strains for both conditions. The divergence in the diamond anvil cell is resolvable when the
493 stresses are at least $P \sim 4$ GPa, $S \sim 0.7$ GPa (although plastic strains are known to occur at lower
494 stresses by the SAXS experiments).
495

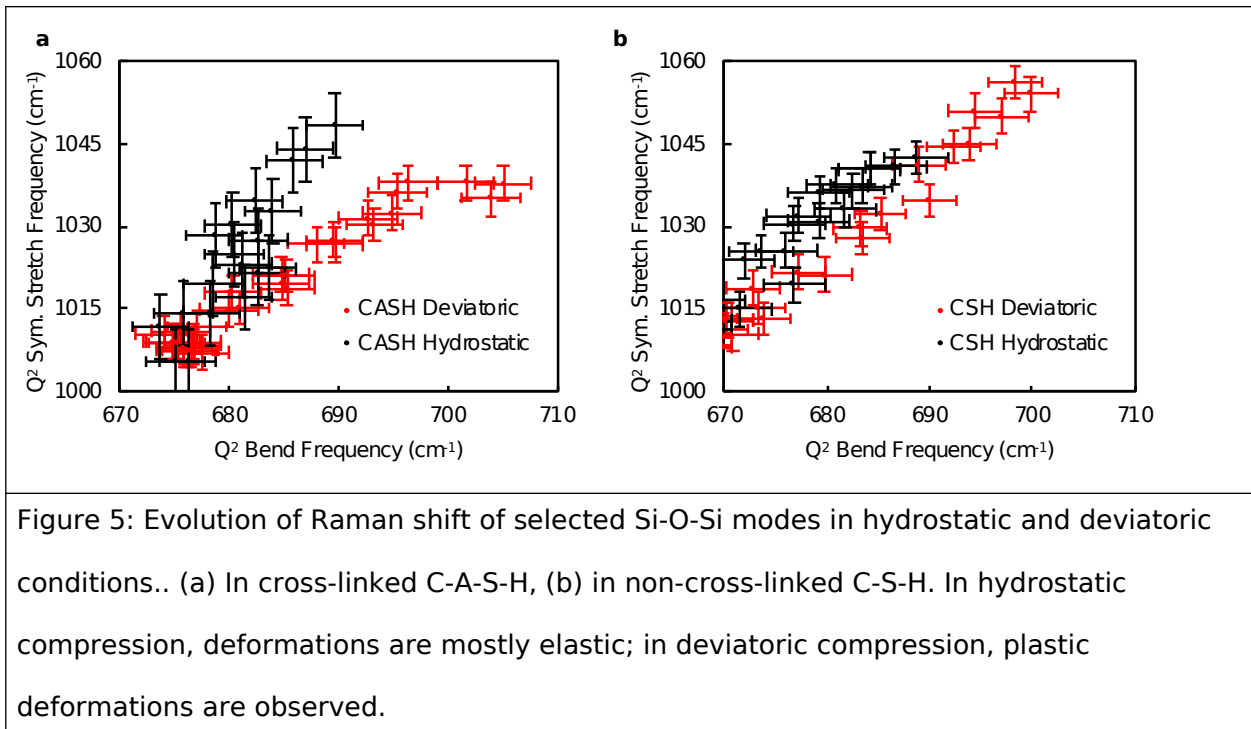


Figure 5: Evolution of Raman shift of selected Si-O-Si modes in hydrostatic and deviatoric conditions.. (a) In cross-linked C-A-S-H, (b) in non-cross-linked C-S-H. In hydrostatic compression, deformations are mostly elastic; in deviatoric compression, plastic deformations are observed.

496
497 One explanation for the divergence is the difference in stress field between the two cases; in the
498 deviatoric case, the c-axis takes more of the total strain, so the bending mode associated with the
499 c-axis should be relatively more strained in the deviatoric case. However, even after accounting
500 for the relative strain in the unit cell axes, the C-A-S-H vibrational modes still diverge (Figures
501 S7e, S7g). In fact, after accounting for the relative unit cell strains, the C-S-H vibrational modes
502 evolve in the same way for both hydrostatic and deviatoric conditions (Figures S7f, h).
503

504 The large divergence in Q² symmetric stretch bond strain in C-A-S-H under deviatoric stress
 505 indicates a relaxation near the Si – O (– Ca) bond. This mode frequency is a qualitative
 506 descriptor of the Si – O bond strain. The bond does not develop more strain under the deviatoric
 507 stress even as the other modes do; an upper bound for the minimum deviatoric stress to achieve
 508 this relaxation is 740 MPa applied to a powder by comparison with the SAXS results above. The
 509 resolution of the high-pressure Raman experiment is not sufficient to detect the relaxation at such
 510 low stresses, but at higher stresses the relaxation is apparent.

Table 2. Vibrational Si-O-Si properties of samples studied in this work.

Sample	Mode	Ambient frequency (cm ⁻¹)	dω/dP, Hydrostatic (cm ⁻¹ /GPa)	dω/dP, Deviatoric (cm ⁻¹ /GPa)
C-A-S-H	Q ² bending	675	2.4	3.6
	Q ² symmetric stretch	1010	6.5	4.2
C-S-H	Q ² bending	669	3.1	4.5
	Q ² symmetric stretch	1012	5.5	5.5

511
 512 We assign the deformation to a slip plane adjacent to the Si – O bonds in C-A-S-H. The
 513 intralayer is the most reasonable motif to slip. This hypothesis is in good agreement with the
 514 comparison to micas and with the surface energy discussion in the Introduction. Breakage of the
 515 Q³ and Q² silica tetrahedra is not favored over the CaO interlayer because Si – O bonds have a
 516 valence unit near 4/4, whereas Ca – O bonds are more like 2/7 or 2/8 [45].
 517

518 The explanation of the bond strain evolution with stress is represented by Figure 6, which is
519 inspired by (i) models of plastic deformation in clays that suppose sheets shear against each other
520 [46] and (ii) a nanomechanical origin of structural strength [47]. At ambient conditions, the
521 powder is isotropic and the unit cell has no deformation (Figures 6a, b). At low compressive
522 stresses the lamellae start to compact and shear against each other [48] (Figures 6c, d).
523 Eventually the stresses cause the lamellae to be sheared apart (Figures 4e, f). Bond strains are
524 qualitatively plotted in Figure 4g for various constituent chemical bonds. From right to left: the
525 O – Ca bonds are softer than Si – O bonds, and suffer greater strains until they slip. The oxygen
526 member of the O – Ca bond is also bonded to a silicon atom, which means that after the slip, the
527 Si – O bond strain does not increase its strain as much (Figure 6g). The Q² bending is unaffected
528 by the slip because it is not party to the bond breaking event.

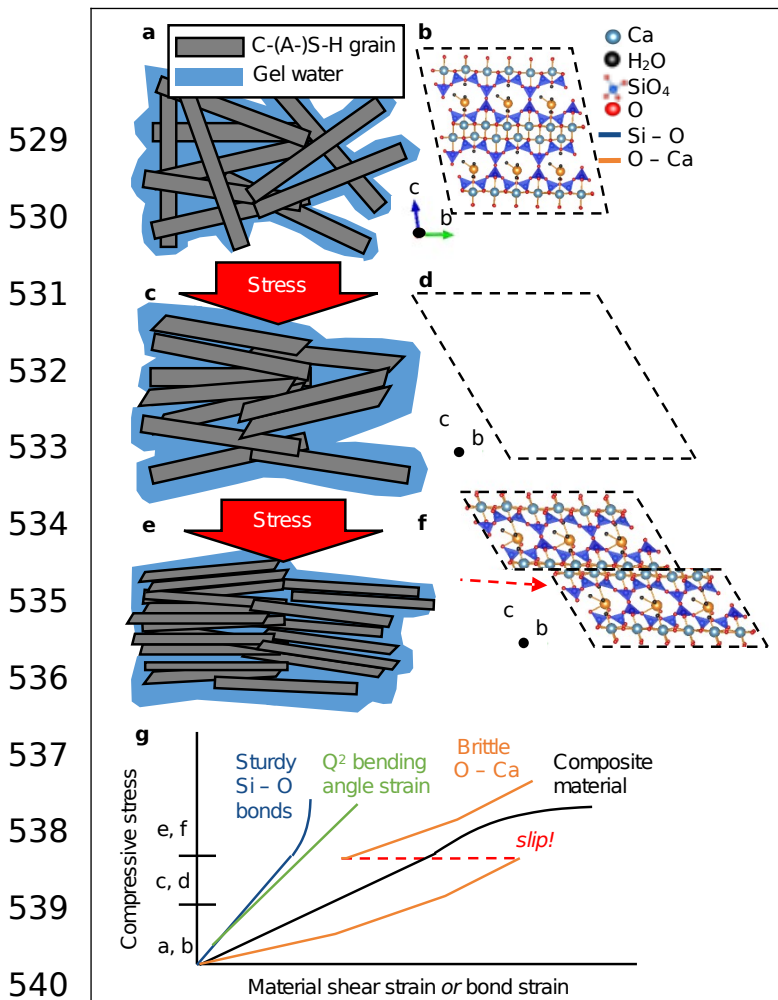


Figure 6: The link between plastic deformations and chemical bonds in C-(A-)S-H. (a) Powder at ambient pressure. (b) Schematic of C-(A-)S-H at ambient pressure. (c) Powder under small deviatoric stress is elastically deformed (d) Unit cell at stress below the material's elastic limit. (e) Powder under large deviatoric stress is plastically deformed, lamellae are broken apart, and preferred orientation develops. (f) Unit cell at stress above the elastic limit, here slipping on the intralayer. (g) Qualitative stress-strain plot of the material and its chemical bonds. Stress axis ticks correspond to the noted part of this figure. The figure is inspired by models of clay compaction[46] and the nanomechanical origins of structural strength[47].

We do not observe any evidence of a deformation or relaxation around the silica tetrahedra modes in the C-S-H sample, so the mechanism that achieved decreased grain thickness must be by a separate mechanism. If the environment around the Si-O-Ca(intralayer) bonds remains nearly isomorphous, as suggested by Figure 5b, then the plane that slips must be the interlayer. Sliding along the interlayer would result in bridging tetrahedra rastering against each other, which would decrease the extent of polymerization and increase the number of Q¹ sites in the structure. Recent characterization of a similar C-S-H sample using X-ray Raman spectroscopy under deviatoric condition with P ~ 20

552 GPa showed a permanent deformation in Ca – O bond length, which was assigned to
553 deformation in both the interlayer and the intralayer [49].

554

555 The Q¹ stretching region in C-S-H grows relative to the Q² stretching region (Table 3, Figure
556 S10). This peak is chosen for normalization because its intensity shows the least dependence on
557 the sample orientation effects [29]. We also examined the compacts by Raman spectroscopy at
558 ambient conditions and at stresses ranging from 240 – 740 MPa, which show the same trend as
559 the powders in the diamond anvil cells. (Figure S11).

560

561 The height ratio is used for comparison because it is more stable compared to the area ratio (the
562 width of the Q¹ peak is highly dependent on the area selected for fitting). Curiously, in the
563 diamond anvil cell and the pellet pressing experiments, the C-S-H Q¹ area increases at low
564 stresses but does not increase at greater applied stresses (Figure S7b, S8b). One possible
565 explanation is that the Q¹ may “scavenge” each other during slip, so that as more are generated
566 by the deviatoric stress, they react with each other when encountered to form Q² in stress-induced
567 polymerization. Silicate polymerization is known to occur when C-(A-)S-H grains are
568 carbonated in air [28].

569

570 The final evidence of plastic deformation in the samples is the growth of the calcium carbonate
571 peak beyond what would be expected from a sample in air (Figure 7). In both samples the
572 calcium carbonate peak grows relative to the Q² peaks. Calcium carbonate grows from accessible
573 calcium atoms and carbon dioxide. Plastic deformation, especially sliding along (004) intralayer,
574 would expose more calcium atoms to carbon dioxide in the air. Over the course of the

575 experiment (three days), the height ratio of CaCO_3 to Q^2 symmetric stretch grows from 0.7 to 1.4
 576 for both samples. In the same powder allowed to react with carbon dioxide in air over ten days,
 577 the ratio only reaches ~ 1 . The excess growth of carbonate phases means that calcium is made
 578 more accessible by the deformation in the DAC.
 579

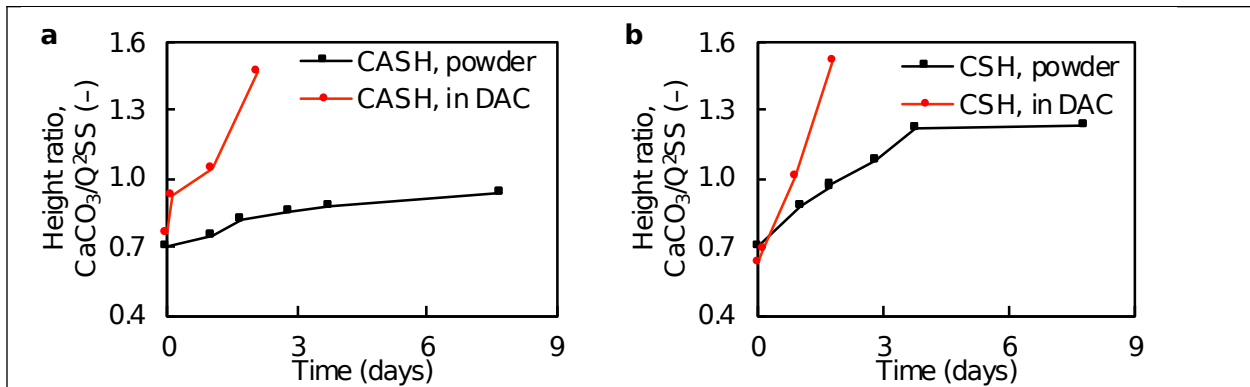


Figure 7: Height ratio of carbonate peak to Q^2 symmetric stretch in (a) C-A-S-H, (b) C-S-H while in the DAC and while in ambient atmosphere. Points are averaged for each day. In the C-A-S-H experiment, uniaxial stress increases to 2.9, 7.5, and 10.0 GPa with each day; in the C-S-H experiment, uniaxial stress increases to 0.3, 3.6, and 9.2 GPa with each day.

580

581

582 3.3 Comparison between SAXS, deviatoric-stress

583 XRD, nanoindentation, and creep

584

585 We do not observe an increase in the Si – O bond strain

586 in C-A-S-H by deviatoric stress Raman spectroscopy (S

587 > 1000 MPa) until much higher deviatoric stress than the

588 compaction experiment ($S \sim 130$ MPa). This may be

Table 3: Relative height of Q^1 peak compared to Q^2 bending peak of powders in diamond anvil cell.

Condition	C-A-S-H	C-S-H
Ambient	0.05	0.06
$S \approx 0.5$ GPa	0.06	0.16
Unload	0.05	0.16

589 because the effect is too subtle to be resolved at lower stresses. We postulate that the C-A-S-H
590 must have a greater resistance to plastic deformation than C-S-H, because if the intralayer was
591 more susceptible than the C-S-H interlayer, then both samples would show minimal Si – O bond
592 strain at high stresses. This is not the case, so the limiting resistance must be higher in C-A-S-H.
593

594 The different mechanisms and active stress regimes we propose are in agreement with creep tests
595 of cross-linked C-A-S-H showing much less creep than C-S-H [16]. The experiments of Ref.
596 [16] compacted non-crosslinked C-S-H and cross-linked C-A-S-H powders into disks using ~500
597 MPa uniaxial stress and performed nanoindentation with an average stress of at least 10's of GPa.
598 Other C-S-H nanoindentation experiments on the same order of stress come close to reproducing
599 the creep behavior of macroscopic concrete [15,17,50]. Because our SAXS and Raman
600 spectroscopy results are obtained at lower stresses than nanoindentation experiments, and
601 nanoindentation experiments reproduce creep behaviour of cements, the plastic deformation
602 mechanisms we observe are likely relevant to extant Portland cements. When an interlayer
603 comprises only water molecules and ions, this is the plane that slips; when the interlayer is
604 bridged by Q³ tetrahedra, the intralayer slips.

605
606 This phenomenon is important when the packing density is so high that intergrain sliding on gel
607 water is not contributing. Inspecting Figure 17 of Ref. [12], a paper that shows the effect of water
608 molecules on the creep of cement using nanoindentation, the condition of high packing density
609 looks to be met for an average water thickness layer of ~5 Å or less, because this is the point at
610 which the effect of fewer water molecules does not seem to correlate with creep compliance.

611 Incidentally this is the same thickness of water in the interlayer of 14 Å tobermorite, a non-cross-
612 linked crystalline analog for C-S-H.

613

614 In practical terms, using the data from Ref. [12], this condition can be met at relative humidity as
615 high as 30%, comparing Ref. [12]'s Figures 9 and 16. In the limit of this model, this means that
616 the creep resistance of cement matrix containing C-(A-)S-H has an upper bound in the durability
617 of the calcium oxide intralayer sheet. Inspecting the scatter that Ref. [12] produces between its
618 samples shows that there is still much room for tuning the creep of cements based on the phases
619 that are formed by the mix.

620

621 More work is still needed to delineate between intragrain slip mechanisms and intergrain sliding,
622 especially with high-pressure X-ray diffraction, to rigorously test whether the mechanisms
623 proposed here are reproduced in real concrete specimens, and the role of other properties of C-
624 (A-)S-H, such as grain size and shape which are known to be important for compaction dynamics
625 [18].

626

627 **4 Conclusions**

628

629 Small angle X-ray scattering of C-A-S-H and C-S-H pellets pressed to 740 MPa shows a
630 decrease in grain thickness from ~70 Å to ~50 Å, while effective grain radii are unchanged in
631 compression. To understand the deformation mechanisms, we used deviatoric-stress Raman
632 spectroscopy of a powder in a diamond anvil cell. This technique shows that in cross-linked C-
633 A-S-H, Si – O bond strain does not increase much at high stresses, indicating a relaxation around

634 Si – O tetrahedra, most likely of the seven-fold-coordinate Ca intralayer. In non-crosslinked C-S-
635 H, bond strains evolve as expected for an isomorphic contraction. Furthermore, this sample
636 shows a relative increase in the area of the Q¹ peak which is attributed to interlayer sliding
637 breaking chains apart.

638

639 This work notes the decrease in average grain thickness of C-A-S-H under 130 MPa deviatoric
640 stress and uses Raman spectroscopy to identify at a chemical-bond-level how the grains
641 plastically deform. The results agree with nanoindentation experiments of similar materials, and
642 the confluence of these results points to intragrain deformation being the dominant mechanism
643 for creep in the cement matrix when the grain edges have less than 5 Å water; this condition is
644 effectively met when the relative humidity is less than 30%. Models of creep and compaction of
645 C-A-S-H must account for this as researchers explore new cement chemistries. More work is
646 needed to understand if the slip planes implicated in this work dominate at all deviatoric stress
647 regimes and what the role of grain size and shape is.

648

649 **Acknowledgements**

650

651 The support of the National Science Foundation under the Division of Materials Research
652 Ceramics Program, DMR-CER, Grant No. 1935604 is gratefully acknowledged. The authors
653 thank Barbara Lothenbach for providing the samples synthesized by Rupert J. Myers at EMPA.

654

655 This material is also based upon work partially supported by the U.S. Department of Energy,
656 Office of Science, Office of Workforce Development for Teachers and Scientists, Office of

657 Science Graduate Student Research (SCGSR) program. The SCGSR program is administered by
658 the Oak Ridge Institute for Science and Education (ORISE) for the DOE. ORISE is managed by
659 ORAU under contract number DE-SC0014664. All opinions expressed in this paper are the
660 author's and do not necessarily reflect the policies and views of DOE, ORAU, or ORISE.

661

662 The Advanced Light Source is supported by the Director, Office of Science, Office of Basic
663 Energy Sciences, of the U.S. Department of Energy under Contract No. DE-AC02-05CH11231.
664 Beamline 12.2.2 and sample preparation of this research are partially supported by COMPRES,
665 the Consortium for Materials Properties Research in Earth Sciences under NSF Cooperative
666 Agreement EAR 1606856.

667

668 **References**

- 669 [1] G. Geng, R.J. Myers, J. Li, R. Maboudian, C. Carraro, D.A. Shapiro, P.J.M. Monteiro,
670 Aluminum-induced dreierketten chain cross-links increase the mechanical properties of
671 nanocrystalline calcium aluminosilicate hydrate, *Sci. Rep.* 7 (2017) 44032. [https://doi.org/
672 10.1038/srep44032](https://doi.org/10.1038/srep44032).
- 673 [2] R.J. Myers, E. L'Hôpital, J.L. Provis, B. Lothenbach, Effect of temperature and
674 aluminium on calcium (alumino)silicate hydrate chemistry under equilibrium conditions,
675 *Cem. Concr. Res.* 68 (2015) 83–93. <https://doi.org/10.1016/j.cemconres.2014.10.015>.
- 676 [3] I.G. Richardson, The calcium silicate hydrates, *Cem. Concr. Res.* 38 (2008) 137–158.
677 <https://doi.org/10.1016/j.cemconres.2007.11.005>.
- 678 [4] J. Li, G. Geng, R. Myers, Y.S. Yu, D. Shapiro, C. Carraro, R. Maboudian, P.J.M.

679 Monteiro, The chemistry and structure of calcium (alumino) silicate hydrate: A study by
680 XANES, ptychographic imaging, and wide- and small-angle scattering, *Cem. Concr. Res.*
681 115 (2019) 367–278. <https://doi.org/10.1016/j.cemconres.2018.09.008>.

682 [5] W.S. Chiang, E. Fratini, P. Baglioni, D. Liu, S.H. Chen, Microstructure determination of
683 calcium-silicate-hydrate globules by small-angle neutron scattering, *J. Phys. Chem. C* 116
684 (2012) 5055–5061. <https://doi.org/10.1021/jp300745g>.

685 [6] R. Taylor, A. Sakdinawat, S.R. Chae, H.R. Wenk, P. Levitz, R. Sougrat, P.J.M. Monteiro,
686 Developments in TEM Nanotomography of Calcium Silicate Hydrate, *J. Am. Ceram. Soc.*
687 98 (2015) 2307–2312. <https://doi.org/10.1111/jace.13585>.

688 [7] A.C.A. Muller, K.L. Scrivener, A.M. Gajewicz, P.J. McDonald, Densification of C-S-H
689 measured by ¹H NMR relaxometry, *J. Phys. Chem. C* 117 (2013) 403–412.
690 <https://doi.org/10.1021/jp3102964>.

691 [8] M. Wyrzykowski, P.J. McDonald, K.L. Scrivener, P. Lura, Water Redistribution within
692 the Microstructure of Cementitious Materials due to Temperature Changes Studied with
693 ¹H NMR, *J. Phys. Chem. C* 121 (2017) 27950–27962.
694 <https://doi.org/10.1021/acs.jpcc.7b08141>.

695 [9] G. Geng, R.N. Vasin, J. Li, M.J.A. Qomi, J. Yan, H.R. Wenk, P.J.M. Monteiro, Preferred
696 orientation of calcium aluminosilicate hydrate induced by confined compression, *Cem.*
697 *Concr. Res.* 113 (2018) 186–196. <https://doi.org/10.1016/j.cemconres.2018.09.002>.

698 [10] H.R. Wenk, P. Van Houtte, Texture and anisotropy, *Reports Prog. Phys.* (2004).
699 <https://doi.org/10.1088/0034-4885/67/8/R02>.

700 [11] A. Morshedifard, S. Masoumi, M.J. Abdolhosseini Qomi, Nanoscale origins of creep in
701 calcium silicate hydrates, *Nat. Commun.* 9 (2018) 1785. <https://doi.org/10.1038/s41467->

- 702 018-04174-z.
- 703 [12] P. Suwanmaneechot, A. Aili, I. Maruyama, Creep behavior of C-S-H under different
704 drying relative humidities: Interpretation of microindentation tests and sorption
705 measurements by multi-scale analysis, *Cem. Concr. Res.* 132 (2020) 106036.
706 <https://doi.org/10.1016/j.cemconres.2020.106036>.
- 707 [13] I. Maruyama, T. Ohkubo, T. Haji, R. Kurihara, Dynamic microstructural evolution of
708 hardened cement paste during first drying monitored by ¹H NMR relaxometry, *Cem.*
709 *Concr. Res.* 122 (2019) 107–117. <https://doi.org/10.1016/j.cemconres.2019.04.017>.
- 710 [14] J. Li, W. Zhang, P.J.M. Monteiro, Preferred orientation of calcium aluminosilicate hydrate
711 compacts: Implications for creep and indentation, *Cem. Concr. Res.* 143 (2021) 106371.
712 <https://doi.org/10.1016/j.cemconres.2021.106371>.
- 713 [15] M. Vandamme, F.-J. Ulm, Nanogranular origin of concrete creep, *Proc. Natl. Acad. Sci.*
714 106 (2009) 10552–10557. <https://doi.org/10.1073/pnas.0901033106>.
- 715 [16] W.A. Hunnicutt, P. Mondal, L.J. Struble, Effect of Aluminum Substitution in C-S-H on
716 Viscoelastic Properties: Stress Relaxation Nanoindentation, in: *1st Int. Conf. Gd.*
717 *Challenges Constr. Mater.*, 2016.
- 718 [17] M. Vandamme, F.J. Ulm, Nanoindentation investigation of creep properties of calcium
719 silicate hydrates, *Cem. Concr. Res.* 52 (2013) 38–52.
720 <https://doi.org/10.1016/j.cemconres.2013.05.006>.
- 721 [18] N. Vandewalle, G. Lumay, O. Gerasimov, F. Ludewig, The influence of grain shape,
722 friction and cohesion on granular compaction dynamics, *Eur. Phys. J. E.* 22 (2007) 241–
723 248. <https://doi.org/10.1140/epje/e2007-00031-0>.
- 724 [19] A.K. Kronenberg, S.H. Kirby, J. Pinkston, Basal slip and mechanical anisotropy of biotite,

725 J. Geophys. Res. 95 (1990) 19257–19278. <https://doi.org/10.1029/jb095ib12p19257>.

726 [20] V.M. Mares, A.K. Kronenberg, Experimental deformation of muscovite, J. Struct. Geol.
727 15 (1993) 1061–1075. [https://doi.org/10.1016/0191-8141\(93\)90156-5](https://doi.org/10.1016/0191-8141(93)90156-5).

728 [21] S.M. Mutisya, C.R. Miranda, The surface stability and morphology of tobermorite 11 Å
729 from first principles, Appl. Surf. Sci. 444 (2018) 287–292.
730 <https://doi.org/10.1016/j.apsusc.2018.03.002>.

731 [22] D. Tunega, A. Zaoui, Understanding of bonding and mechanical characteristics of
732 cementitious mineral tobermorite from first principles, J. Comput. Chem. 32 (2011) 306–
733 314. <https://doi.org/10.1002/jcc.21622>.

734 [23] F. Puertas, M. Palacios, H. Manzano, J.S. Dolado, A. Rico, J. Rodríguez, A model for the
735 C-A-S-H gel formed in alkali-activated slag cements, J. Eur. Ceram. Soc. 31 (2011) 2043–
736 2056. <https://doi.org/10.1016/j.jeurceramsoc.2011.04.036>.

737 [24] J. Ilavsky, Nika: Software for two-dimensional data reduction, J. Appl. Crystallogr. 45
738 (2012) 324–328. <https://doi.org/10.1107/S0021889812004037>.

739 [25] M. Kroon, W.L. Vos, G.H. Wegdam, Structure and formation of a gel of colloidal disks,
740 Phys. Rev. E - Stat. Physics, Plasmas, Fluids, Relat. Interdiscip. Top. 19 (1998) 887–894.
741 <https://doi.org/10.1103/PhysRevE.57.1962>.

742 [26] B. Hammouda, A new Guinier-Porod model, J. Appl. Crystallogr. 43 (2010) 719.
743 <https://doi.org/10.1107/S0021889810015773>.

744 [27] R.A. Vaia, W. Liu, H. Koerner, Analysis of small-angle scattering of suspensions of
745 organically modified montmorillonite: Implications to phase behavior of polymer
746 nanocomposites, J. Polym. Sci. Part B Polym. Phys. 41 (2003) 3214–3236. <https://doi.org/10.1002/polb.10698>.

747

- 748 [28] S. Ortaboy, J. Li, G. Geng, R.J. Myers, P.J.M. Monteiro, R. Maboudian, C. Carraro,
749 Effects of CO₂ and temperature on the structure and chemistry of C-(A-)S-H
750 investigated by Raman spectroscopy, *RSC Adv.* 7 (2017) 48925–48933.
751 <https://doi.org/10.1039/C7RA07266J>.
- 752 [29] D.W. Gardner, J. Li, S. Masoumi, M.J.A. Qomi, P.J.M. Monteiro, R. Maboudian, C.
753 Carraro, Silicate Bond Characteristics in Calcium-silicate-hydrates Determined by High
754 Pressure Raman Spectroscopy, *J. Phys. Chem. C.* 124 (2020) 18335–18345.
- 755 [30] R.J. Kirkpartick, J.L. Yarger, P.F. McMillan, P. Yu, X. Cong, Raman spectroscopy of C-
756 S-H, tobermorite, and jennite, *Adv. Cem. Based Mater.* 5 (1997) 93–99.
757 [https://doi.org/10.1016/S1065-7355\(97\)00001-1](https://doi.org/10.1016/S1065-7355(97)00001-1).
- 758 [31] L. Black, C. Breen, J. Yarwood, K. Garbev, P. Stemmermann, B. Gasharova, Structural
759 features of C-S-H(I) and its carbonation in air-A Raman spectroscopic study. Part II:
760 Carbonated phases, *J. Am. Ceram. Soc.* 90 (2007) 908–917.
761 <https://doi.org/10.1111/j.1551-2916.2006.01429.x>.
- 762 [32] K. Garbev, P. Stemmermann, L. Black, C. Breen, J. Yarwood, B. Gasharova, Structural
763 features of C-S-H(I) and its carbonation in air-A Raman spectroscopic study. Part I: Fresh
764 phases, *J. Am. Ceram. Soc.* 90 (2007) 900–907. [https://doi.org/10.1111/j.1551-](https://doi.org/10.1111/j.1551-2916.2006.01428.x)
765 [2916.2006.01428.x](https://doi.org/10.1111/j.1551-2916.2006.01428.x).
- 766 [33] G. Renaudin, J. Russias, F. Leroux, C. Cau-dit-Coumes, F. Frizon, Structural
767 characterization of C-S-H and C-A-S-H samples-Part II: Local environment investigated
768 by spectroscopic analyses, *J. Solid State Chem.* 182 (2009) 3320–3329.
769 <https://doi.org/10.1016/j.jssc.2009.09.024>.
- 770 [34] G. Geng, R.J. Myers, M.J.A. Qomi, P.J.M. Monteiro, Densification of the interlayer

- 771 spacing governs the nanomechanical properties of calcium-silicate-hydrate, *Sci. Rep.* 7
772 (2017) 1–8. <https://doi.org/10.1038/s41598-017-11146-8>.
- 773 [35] M. Chai, J.M. Brown, Effects of static non-hydrostatic stress on the R lines of ruby single
774 crystals, *Geophys. Res. Lett.* 23 (1996) 3539–3542. <https://doi.org/10.1029/96GL03372>.
- 775 [36] A.K. Singh, The lattice strains in a specimen (cubic system) compressed
776 nonhydrostatically in an opposed anvil device, *J. Appl. Phys.* 73 (1993) 4278–4286.
777 <https://doi.org/10.1063/1.352809>.
- 778 [37] A.K. Singh, C. Balasingh, The lattice strains in a specimen (hexagonal system)
779 compressed nonhydrostatically in an opposed anvil high pressure setup, *J. Appl. Phys.* 75
780 (1994) 4956–4962. <https://doi.org/10.1063/1.355786>.
- 781 [38] A.M. Hofmeister, H. -k. Mao, Redefinition of the mode Grüneisen parameter for
782 polyatomic substances and thermodynamic implications, *Proc. Natl. Acad. Sci.* 99 (2002)
783 559–564. <https://doi.org/10.1073/pnas.241631698>.
- 784 [39] Y. Sato, S.I. Akimoto, Hydrostatic compression of four corundum-type compounds: α -Al
785 $2O_3$, V_2O_3 , Cr_2O_3 , and α - Fe_2O_3 , *J. Appl. Phys.* 50 (1979) 5285–5291.
786 <https://doi.org/10.1063/1.326625>.
- 787 [40] J. Chappuis, A new model for a better understanding of the cohesion of hardened
788 hydraulic materials, *Colloids Surfaces A Physicochem. Eng. Asp.* 156 (1999) 223–241.
789 [https://doi.org/10.1016/S0927-7757\(99\)00075-8](https://doi.org/10.1016/S0927-7757(99)00075-8).
- 790 [41] S.D. Palkovic, S. Yip, O. Büyüköztürk, A cohesive-frictional force field (CFFF) for
791 colloidal calcium-silicate-hydrates, *J. Mech. Phys. Solids.* 109 (2017) 160–177.
792 <https://doi.org/10.1016/j.jmps.2017.08.012>.
- 793 [42] A. Moshiri, D. Stefaniuk, S.K. Smith, A. Morshedifard, D.F. Rodrigues, M.J.A. Qomi,

- 794 K.J. Krakowiak, Structure and morphology of calcium-silicate-hydrates cross-linked with
795 dipodal organosilanes, *Cem. Concr. Res.* 133 (2020) 106076.
796 <https://doi.org/10.1016/j.cemconres.2020.106076>.
- 797 [43] R.P.S. Fartaria, N. Javid, J. Sefcik, M.B. Sweatman, Simulation of scattering and phase
798 behavior around the isotropic-nematic transition of discotic particles, *J. Colloid Interface*
799 *Sci.* 377 (2012) 94–104. <https://doi.org/10.1016/j.jcis.2012.03.046>.
- 800 [44] R. Eppenga, D. Frenkel, Monte carlo study of the isotropic and nematic phases of
801 infinitely thin hard platelets, *Mol. Phys.* 52 (1984) 1303–1334.
802 <https://doi.org/10.1080/00268978400101951>.
- 803 [45] E.J. Tarbuck, F.K. Lutgens, *Essentials of Geology 11th Edition, Earth an Introd. to Phys.*
804 *Geol.* (1984). [https://doi.org/10.1016/0031-9201\(74\)90065-x](https://doi.org/10.1016/0031-9201(74)90065-x).
- 805 [46] Z.P. Bažant, J.K. Kim, Creep of anisotropic clay: Microplane model, *J. Geotech. Eng.* 112
806 (1986) 458–475. [https://doi.org/10.1061/\(ASCE\)0733-9410\(1986\)112:4\(458\)](https://doi.org/10.1061/(ASCE)0733-9410(1986)112:4(458)).
- 807 [47] J.L. Le, Z.P. Bažant, M.Z. Bazant, Unified nano-mechanics based probabilistic theory of
808 quasibrittle and brittle structures: I. Strength, static crack growth, lifetime and scaling, *J.*
809 *Mech. Phys. Solids.* 59 (2011) 1291–1321. <https://doi.org/10.1016/j.jmps.2011.03.002>.
- 810 [48] S. Strijbos, P.J. Rankin, R.J. Klein Wassink, J. Bannink, G.J. Oudemans, Stresses
811 occurring during one-sided die compaction of powders, *Powder Technol.* 18 (1977) 187–
812 200. [https://doi.org/10.1016/0032-5910\(77\)80008-9](https://doi.org/10.1016/0032-5910(77)80008-9).
- 813 [49] J. Li, W. Zhang, P.J.M. Monteiro, Synchrotron X-ray Raman scattering shows the changes
814 of the Ca environment in C-S-H exposed to high pressure, *Cem. Concr. Res.* 132 (2020)
815 106066. <https://doi.org/10.1016/j.cemconres.2020.106066>.
- 816 [50] K. Ioannidou, K.J. Krakowiak, M. Bauchy, C.G. Hoover, E. Masoero, S. Yip, F.-J. Ulm,

817 P. Levitz, R.J.-M. Pellenq, E. Del Gado, Mesoscale texture of cement hydrates, Proc. Natl.
818 Acad. Sci. 113 (2016) 2029–2034. <https://doi.org/10.1073/pnas.1520487113>.

819

820 **Competing Interests**

821

822 The authors declare no competing interests.